Optics Letters

Noninvasive, *in vivo* rodent brain optical coherence tomography at 2.1 microns

Jun Zhu,[1] Shau Poh Chong,[1] Wenjun Zhou,[1] and Vivek J. Srinivasan[1,2,*]

[1]Biomedical Engineering Department, University of California Davis, Davis, California 95616, USA
[2]Department of Ophthalmology and Vision Science, School of Medicine, University of California Davis, Sacramento, California 95817, USA
*Corresponding author: vjsriniv@ucdavis.edu

Received 9 May 2019; revised 6 July 2019; accepted 16 July 2019; posted 17 July 2019 (Doc. ID 365725); published 22 August 2019

In biological tissue, longer near-infrared wavelengths generally experience less scattering and more water absorption. Here we demonstrate an optical coherence tomography (OCT) system centered at 2.1 microns, whose bandwidth falls in the 2.2 micron water absorption optical window, for *in vivo* imaging of the rodent brain. We show *in vivo* that at 2.1 microns, the OCT signal is actually attenuated less in cranial bone than at 1.3 microns, and is also less susceptible to multiple scattering tails. We also show that the 2.2 micron window enables direct spectroscopic OCT assessment of tissue water content. We conclude that with further optimization, 2.2 micron OCT will have advantages in low-water-content tissue such as bone, as well as applications where extensive averaging is possible to compensate absorption losses.

https://doi.org/10.1364/OL.44.004147

Looking deeper into biological tissue with high resolution is a fundamental goal of biophotonics. Yet, tissue scattering and absorption [1] limit the achievable imaging depth. While the scattering coefficient (μ_s) decreases at longer wavelengths, the absorption coefficient (μ_a) generally increases [2]. Water absorption locally drops within near-infrared (NIR) optical windows located around 1.05, 1.3, 1.7, and 2.2 μm [3]. The ballistic attenuation coefficient ($\mu_s + \mu_a$) is also locally minimized within each of these windows. In optical coherence tomography (OCT), longer wavelengths are of particular interest, even though water absorption is higher, since less scattering implies that a higher fraction of the detected OCT signal comprises single backscattering paths, as opposed to multiply scattered paths. The window at 1.3 μm is often used in OCT due to the availability of high-performance telecommunication components. Though used less often, the 1.7 μm optical window has even lower scattering, and attains the lowest attenuation coefficient for deep microscopy in tissues such as the brain [2,4–6]. The NIR optical window around 2.2 μm is even more rarely used for tissue imaging because of light source limitations [7] and high water absorption [8]. However, the benefits of 2.2 μm for *in vivo* imaging through bone, a biological tissue with moderate water mass content (12% [9]) compared to other tissues (>70% [10]), have not been investigated, to our knowledge.

Here, we describe 2.1 μm spectral domain OCT for noninvasive *in vivo* rodent brain imaging. Importantly, we show that attenuation in the skull is actually lower at 2.1 μm than at 1.3 μm, a conventional NIR window. We further demonstrate cortical OCT angiography in rats through the intact skull at 2.1 μm. In addition to the anticipated reduction in multiply scattered light, our results highlight additional advantages of the 2.2 μm spectral window for *in vivo* OCT: lower attenuation in bone and direct spectroscopic assessment of water content.

The 2.1 μm OCT system configuration is shown in Fig. 1A. A supercontinuum light source (SuperK Extreme EXR20, NKT Photonics) was filtered by two bandpass filters (BBP-1615-2280, Spectrogon; FB2250-500, Thorlabs, Inc.), and coupled by a reflective collimator (RC02, Thorlabs, Inc.) into a customized 50/50 SM2000 fiber coupler (Thorlabs, Inc.). In the sample arm, the beam was collimated by a reflective collimator (RC04, Thorlabs, Inc.), scanned by a 2D galvanometer (GVS002, Thorlabs, Inc.), and then focused onto the sample by a scan lens (LSM02 or LSM03, Thorlabs, Inc.). In the reference arm, an adjustable iris varied the reference power, and a glass slab compensated the sample arm dispersion. The backscattered light from the sample and light reflected from the reference mirror were recombined by the fiber coupler and relayed to a custom spectrometer. In the spectrometer, the beam was collimated by a 90° off-axis parabolic mirror (MPD249-P01, Thorlabs, Inc.), dispersed by a diffraction grating (600 lines per millimeter, Wasatch Photonics), focused by a 150 mm effective focal length achromatic doublet pair (Thorlabs, Inc.), and detected by an extended InGaAs line scan camera (SU1024LDH-2.2RT, Sensors Unlimited). The camera was externally triggered and synchronized with 2D galvanometer scanning. Data were collected via the frame grabber (PCIe-1427, National Instruments Corp.). All the hardware control was performed by a custom LabVIEW program. The spectrometer spectral range was 1990–2210 nm (Fig. 1B). The sensitivity roll-off was less than 5 dB over the first half of the imaging range (Fig. 1C). The measured axial resolution in air was 18.6 μm (14.0 μm in water) (Fig. 1D). A $1/e^2$ transverse resolution of 16/32 μm (LSM02/LSM03) on the sample was achieved. The maximum sensitivity was ~84 dB with 4.3 mW incident power and a 14.1 μs (47 kHz line rate) camera exposure time.

System noise sources were characterized by varying the reference power/photoelectron number captured by the camera [11]. For each pixel in the line scan camera, total noise versus detected photoelectron number was fitted with a quadratic function, and the second-order nonlinear term, first-order linear term, and the constant term were assigned to excess noise, shot noise, and detector noise, respectively. System sensitivity relative to the shot noise limit (SNL) was analyzed when the camera was operated with small (1.25 Me^-)/large (12.5 Me^-) full well capacity (FWC), and short (14.1 μs, 47 kHz line rate)/long (79.9 μs, 12 kHz line rate) exposure (EXP) time modes (Fig. 1E). The maximum system sensitivity relative to SNL was around 3.2%, limited by high detector noise and light source excess noise (Fig. 1F).

Despite the limited system performance, we proceeded to investigate the potential benefits of the 2.2 μm window by comparing rodent brain imaging with our 2.1 μm system and a previously described 1.3 μm system [12], through the intact skull.

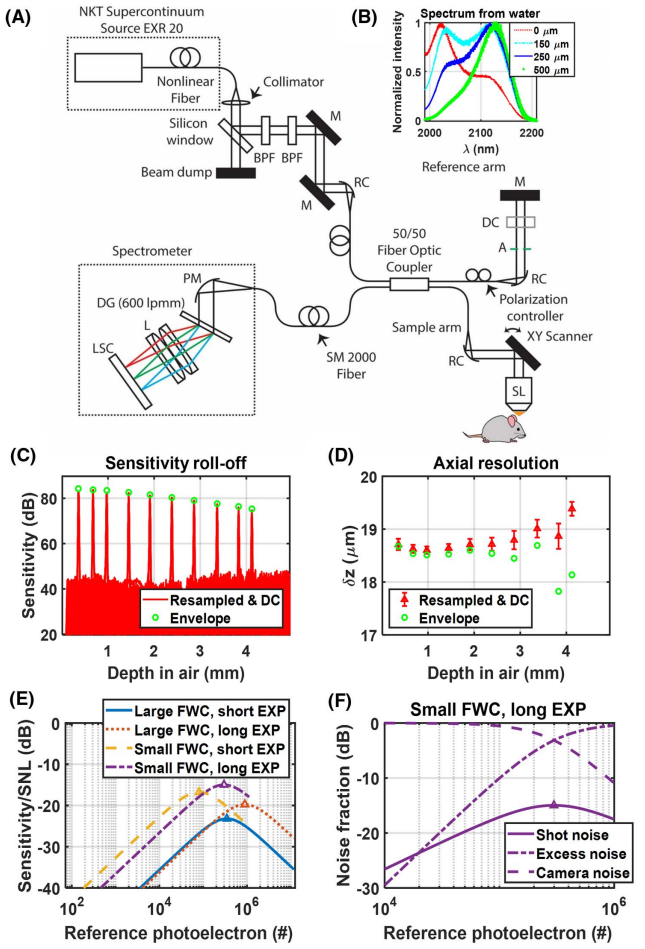

Fig. 1. (A) Schematic of the 2.1 μm OCT system (BPF, bandpass filter; M, mirror; RC, reflective collimator; SL, scan lens; A, aperture; DC, dispersion compensation glass; PM, parabolic mirror; DG, diffraction grating; L, lens; LSC, line scan camera). (B) Spectra from different depths in water with the reference spectrum at 0 μm. (C) Sensitivity roll-off and (D) axial resolution versus depth with dispersion compensation (DC), compared to values obtained from the fringe envelope (circles). (E) System sensitivity, relative to the shot noise limit, using different operation modes of the camera (SNL, shot noise limit; FWC, full well capacity; EXP, camera exposure time). (F) Fractional contributions of different noise sources using the small FWC, long EXP mode.

Long-Evans (rats #1–2) and Sprague-Dawley (rats #3–5) rats (male, 200–300 g, Charles River) were anesthetized with isoflurane (1.5–2.5% v/v) in a gas mixture of 80% medical air and 20% oxygen, delivered continuously during the experiments. After anesthesia induction, rats were fixed in a stereotactic frame (Stoelting Co.). The scalp was removed carefully with the skull intact. A coverslip was affixed to the skull with superglue (Vibra-Tite), and the imaged field-of-view was 2×2 mm^2/2.5×2.5 mm^2. All experimental procedures and setup were approved by UC Davis Institutional Animal Care and Use Committee. The incident sample power was 3.5/4.3 mW with scan lens LSM02/LSM03. Volumes, denoted as $X \times Y$, were acquired with X axial scans × Y frames, with frame repeats for averaging and angiography. The acquired fringes were resampled, dispensation compensated, and Fourier transformed to yield the complex OCT data. To provide an intrinsic comparison of the two optical windows, irrespective of OCT system performance, intensity (modulus squared of complex data) images were corrected for the depth-dependent noise background and sensitivity roll-off. Volumetric data within each sublocation were flattened based on the segmented skull surface and then averaged transversally to yield line profiles. Refractive indices of $n_{skull} = 1.5$ and $n_{cortex} = 1.33$ were assumed for quantitative attenuation coefficient analysis.

Cross-sectional images of the cranium and cortex, acquired by sequential 1.3 μm [512 × 512 (19 repeats)] and 2.1 μm [640 × 640 (19 repeats)] OCT of the same rat (Figs. 2A and 2B, respectively, $n = 1.33$ used for image display), illustrate different attenuation characteristics in skull versus brain (Fig. 2C). The field-of-view was then divided into nine subregions for total attenuation coefficient measurements, and confocal gating [13] was accounted for as follows:

$$I(z,\lambda) = C\left\{\left[\frac{z - z_{cf}(\lambda)}{z_0(\lambda)}\right]^2 + 1\right\}^{-1} e^{-2\mu_t(\lambda)z}, \quad (1)$$

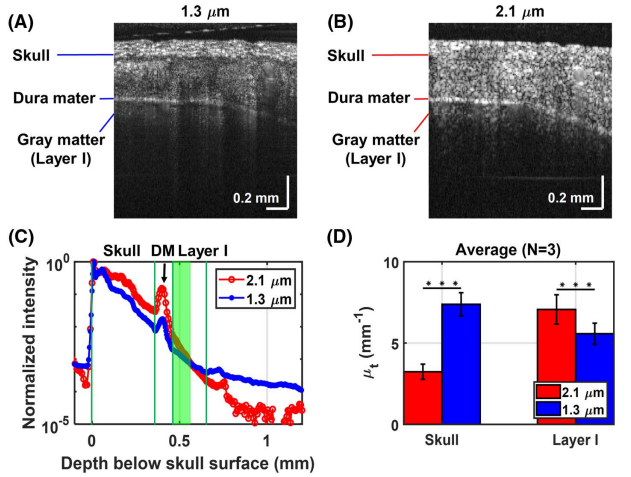

Fig. 2. Cross-sectional images of the rat cranium and cortex with (A) 1.3 μm and (B) 2.1 μm systems. (C) Tissue OCT signal line profiles, with boundaries of skull and cortical layer I delimited by green lines (DM, dura mater). The green shaded area represents fitted range of cortical layer I. (D) Average tissue attenuation coefficients (mean± standard deviation) of rats #1–3. Horizontal lines indicate statistically significant differences determined by two-way ANOVA. $P < 0.001$ (***).

where z is depth, $I(z,\lambda)$ represents OCT line profile, $z_0(\lambda)$ is the Gaussian beam Rayleigh range, and $z_{cf}(\lambda)$ denotes the depth location of the beam waist, set to the approximate focus location. The OCT signal attenuation was described by an exponential decay term, where the factor of 2 accounts for double-pass attenuation, and C is a constant. Attenuation coefficients in superficial cortical layer I (green shaded area in Fig. 2C) across 27 subregions among the three rats were compared (Fig. 2D). Statistical significance was determined by two-way ANOVA, treating wavelength and subject as effects. In the skull, the OCT signal attenuates less rapidly at 2.1 μm than at 1.3 μm ($P < 0.001$) due to lower scattering, while in cortical layer I, which has high water content, absorption is more severe, and the attenuation coefficient at 2.1 μm is larger ($P < 0.001$).

We further noticed that water absorption decreases significantly across our spectral range (1990–2210 nm). This feature might enable the spectroscopic assessment of water volume fraction (proportional to water content), provided that scattering is treated properly. Thus, we divided the spectrum into seven subbands, with central wavelengths of 2009, 2037, 2065, 2094, 2123, 2154, and 2186 nm and full width at half-maximum of ~36 nm. In each subregion of the imaged field-of-view, the background and sensitivity roll-off corrected, locally flattened, and transversally averaged OCT signal, $I(z,\lambda)$, was then fitted with a combined model of confocal gating and single scattering,

$$I(z,\lambda) = C\left\{\left[\frac{z-z_{cf}(\lambda)}{z_0(\lambda)}\right]^2+1\right\}^{-1} e^{-2\left[A\left(\frac{\lambda}{500}\right)^{-b}+f_w\mu_{a,w}(\lambda)\right]z}. \quad (2)$$

Here, the chromatic focal shift between subbands was included in $z_{cf}(\lambda)$. The attenuation coefficient $\mu_t(\lambda)$ is the sum of scattering attenuation $[\mu_{t,s}(\lambda) = A(\lambda/500)^{-b}$, which, unlike μ_s, includes multiple scattering effects] [1] and water absorption $[f_w\mu_{a,w}(\lambda)]$, where b is the scattering power and f_w is water volume fraction. As b is sample-dependent and unknown *a priori*, it was sequentially fixed at assumed values from 0 to 1.5, while C, f_w, and A were fitted using nonlinear least squares regression for each assumed b.

Based on the model in Eq. (2), water volume fraction (f_w) was estimated (Fig. 3). To first assess the methodology, *ex vivo* phantom experiments were performed. Figure 3A shows fitting of the normalized OCT signal in each subband of a 25% (v/v) intralipid-20 (IL-20) solution (diluted by deionized water). Assuming a scattering power of 0.5, fitted total attenuation coefficients (red in Fig. 3B) follow water absorption (blue dashed line) across the spectrum, suggesting high water content. Attenuation is dominated by absorption $[f_w\mu_{a,w}(\lambda)]$ (blue), not scattering $[\mu_{t,s}(\lambda) = A(\lambda/500)^{-b}]$ (green). As the assumed b value varies from 0 to 1.5, the estimated f_w of the IL-20 solution varies from 94.1 to 91.5% (Fig. 3C), which is close to the estimated value of 94.3% [0.25 × (1 − 22.7%) + 0.75], assuming a 22.7% volume fraction of scattering particles in pure IL-20 [14]. Figure 3D shows fitting of the normalized OCT signal in each subband of a dry optical diffuser (WS-1, Ocean Optics). Assuming a scattering power of 0.5, fitted attenuation coefficients (Fig. 3E) change little across the spectrum, suggesting low water content. As the assumed b value varies from 0 to 1.5, the estimated f_w varies from 9.8 to −6.5% (Fig. 3F). Nonphysical negative f_w values are returned by the fitting routine to compensate large attenuation variations with larger assumed b.

Given these reasonable results in phantoms, we then segmented and analyzed the rat skull and brain cortical layer I *in vivo*, applying the model in Eq. (2) and assuming that water is the main absorber in skull [15] and cortex in our wavelength range. For *in vivo* analysis, the longest wavelength subband was discarded due to poor cortical sensitivity, limited by detector quantum efficiency. Fitting of the normalized, *in vivo* OCT signal in the rat skull (Fig. 3G) and superficial cortical layer I (Fig. 3J) reveals that, assuming a reasonable scattering power of 0.5, fitted total attenuation coefficients across the spectrum change less in the skull (Fig. 3H) than in layer I (Fig. 3K), suggesting lower water content in skull. Accordingly, *in vivo* fitting (Figs. 3I and 3L) estimates that cortical layer I has a higher water volume fraction (60–70%) compared to the skull (~20%).

En face angiograms (based on interframe complex OCT signal subtraction followed by intensity averaging) of the rat cranium and cortex acquired by the 1.3 [640 × 640 (9 repeats)] and 2.1 μm [640 × 640 (18 repeats)] systems (Figs. 4A and 4B, respectively; $n = 1.33$ used for image display) were similar. As transverse resolutions (15 and 16 μm, respectively) were closely matched, the comparable image quality, in spite of the suboptimal 2.1 μm OCT system performance, is notable. To assess multiple scattering, after locally flattening and averaging the

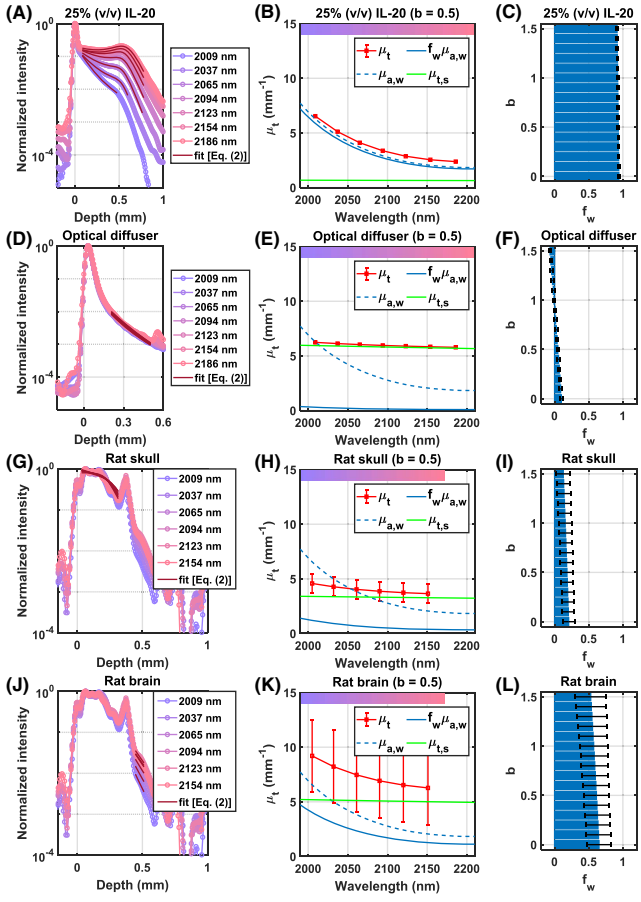

Fig. 3. Spectroscopic measurements of water volume fraction based on absorption. (A, D, G, J) Normalized OCT subband line profiles for 25% (v/v) IL-20 solution, dry optical diffuser, skull, and brain (rat #2). Line profile fits (dark solid lines) are based on Eq. (2). (B, E, H, K) Wavelength-dependent fitted attenuation coefficients (μ_t) (red) are determined as the sum of fitted absorption attenuation ($f_w\mu_{a,w}$) (blue) and fitted scattering attenuation ($\mu_{t,s}$) (green), assuming a scattering power, b, of 0.5. Pure water absorption ($\mu_{a,w}$) is shown for reference (blue dashed line). (C, F, I, L) Estimated water volume fraction (f_w) depends weakly on assumed b. Error bars indicate standard deviations.

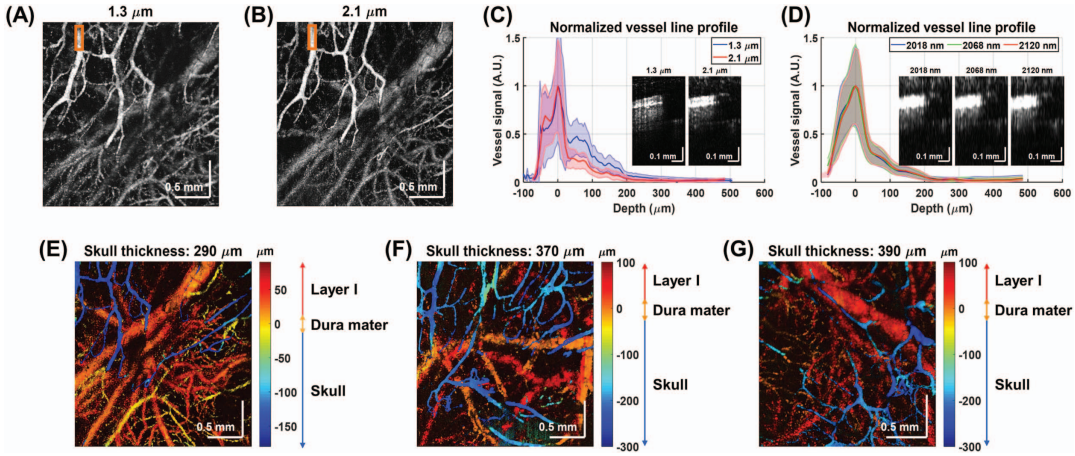

Fig. 4. *En face* angiograms of rat cranium and cortex acquired by (A) 1.3 μm and (B) 2.1 μm OCT systems. (C) Skull vessel line profiles in an ROI (orange box) reveal diminished tails at 2.1 μm, as confirmed by cross-sectional angiograms within the ROI at the two wavelengths (insets). (D) Subband skull vessel line profiles within the ROI are similar from 2.02–2.12 μm, as seen in cross-sectional angiograms within the ROI (insets). (E–G) Depth (distance to the dura mater) color-coded *en face* angiograms of rats with different skull thicknesses (rats #2 and #4–5). Note that the assumed refractive index in C and D is $n = 1.33$, while in E–G, $n_{\text{skull}} = 1.5$ and $n_{\text{cortex}} = 1.33$.

angiograms, normalized skull vessel line profiles from the orange region-of-interest (ROI) at 1.3 and 2.1 μm are compared in Fig. 4C (example cross-sectional angiogram insets). In the line profiles, the vessel lumen is from −60 to 30 μm while the multiple scattering tails [16] start around 30 μm. Overall, across six similar ROIs, the magnitude of tails at 2.1 μm is 41 ± 9% lower than at 1.3 μm. Moreover, the skull vessel line profiles of subband angiograms from 2.02–2.12 μm are similar (Fig. 4D), indicating that water absorption is not the main factor in this finding. Rather, lower scattering around 2.1 μm likely explains the lower tail magnitude. Depth color-coded *en face* angiograms of rats #2 and #4–5 at 2.1 μm (Figs. 4E–4G) show skull vessels above the dura mater in blue, and cortical vessels in red (distance to dura mater calculated with $n_{\text{skull}} = 1.5$ and $n_{\text{cortex}} = 1.33$). Superficial cortical vasculature is resolved through the intact skull.

Currently, system sensitivity is highly limited due to detector and light source noise. Also, the extended InGaAs camera used here had a cutoff at 2.2 μm, the center of the NIR optical window of interest. Furthermore, not all optical components used were optimized for 2.1 μm, further reducing sensitivity. For instance, the scan lens (LSM02/LSM03) in the sample arm has 64%/42% double-pass loss. Customized optics would improve the maximal sensitivity. The sensitivity could also be improved by a swept source system with lower losses and dual-balanced detection. A shot-noise-limited, low-loss system could achieve >100 dB sensitivity. For skull water content, the potential role of collagen absorption merits further investigation. Also, a cortical water volume fraction of 60–70% is slightly lower than expected. In the future, weighting of water absorption coefficients to account for the finite spectral width of each subband can improve quantitative accuracy. Better *a priori* information about scattering power would also improve accuracy.

In summary, a novel OCT microscope operating in the 2.2 μm spectral window was demonstrated for noninvasive *in vivo* imaging of the rodent brain. Though 2.2 μm is not often used for biological imaging due to high water absorption, we showed *in vivo* that for bone, a low water content biological tissue, 2.1 μm actually has lower OCT attenuation than 1.3 μm. Despite limited system performance, intrinsic benefits of the 2.2 μm window were identified, including lower cranial bone attenuation, more immunity to multiple scattering, and the ability to spectroscopically quantify tissue water content.

Funding. National Institutes of Health (NIH) (EB023591, EY028287, NS094681, NS105043).

Acknowledgment. We thank Dr. Alfredo Dubra (Stanford University) for material support.

REFERENCES

1. S. L. Jacques, Phys. Med. Biol. **58**, R37 (2013).
2. L. Shi, L. A. Sordillo, A. Rodríguez-Contreras, and R. Alfano, J. Biophotonics **9**, 38 (2016).
3. L. Shi and R. R. Alfano, *Deep Imaging in Tissue and Biomedical Materials: Using Linear and Nonlinear Optical Methods* (Pan Stanford, 2017).
4. N. G. Horton, K. Wang, D. Kobat, C. G. Clark, F. W. Wise, C. B. Schaffer, and C. Xu, Nat. Photonics **7**, 205 (2013).
5. S. P. Chong, C. W. Merkle, D. F. Cooke, T. Zhang, H. Radhakrishnan, L. Krubitzer, and V. J. Srinivasan, Opt. Lett. **40**, 4911 (2015).
6. M. Yamanaka, T. Teranishi, H. Kawagoe, and N. Nishizawa, Sci. Rep. **6**, 31715 (2016).
7. H. Liang, R. Lange, B. Peric, and M. Spring, Appl. Phys. B **111**, 589 (2013).
8. D. M. Wieliczka, S. Weng, and M. R. Querry, Appl. Opt. **28**, 1714 (1989).
9. D. White, E. Widdowson, H. Woodard, and J. Dickerson, Br. J. Radiol. **64**, 149 (1991).
10. R. F. Reinoso, B. A. Telfer, and M. Rowland, J. Pharmacol. Toxicol. Methods **38**, 87 (1997).
11. S. P. Chong, M. Bernucci, H. Radhakrishnan, and V. J. Srinivasan, Biomed. Opt. Express **8**, 323 (2017).
12. C. W. Merkle, C. Leahy, and V. J. Srinivasan, Biomed. Opt. Express **7**, 4289 (2016).
13. D. J. Faber, F. J. Van Der Meer, M. C. Aalders, and T. G. van Leeuwen, Opt. Express **12**, 4353 (2004).
14. B. Aernouts, E. Zamora-Rojas, R. Van Beers, R. Watté, L. Wang, M. Tsuta, J. Lammertyn, and W. Saeys, Opt. Express **21**, 32450 (2013).
15. M. N. Islam, "Near-infrared super-continuum lasers for early detection of breast and other cancers," U.S. patent 9,993,159 (June12, 2018).
16. M. T. Bernucci, C. W. Merkle, and V. J. Srinivasan, Biomed. Opt. Express **9**, 1020 (2018).